Energy & Environmental Science

PAPER

View Article Online
View Journal | View Issue

Cite this: *Energy Environ. Sci.*, 2018, **11**, 2550

Selective CO_2 reduction to C_3 and C_4 oxyhydrocarbons on nickel phosphides at overpotentials as low as 10 mV†

Karin U. D. Calvinho, ‡[a] Anders B. Laursen, ‡[a] Kyra M. K. Yap,[a] Timothy A. Goetjen,[a] Shinjae Hwang,[a] Nagarajan Murali,[a] Bryan Mejia-Sosa,[b] Alexander Lubarski,[a] Krishani M. Teeluck,[a] Eugene S. Hall,[a] Eric Garfunkel,[a] Martha Greenblatt[a] and G. Charles Dismukes *[ab]

Received 31st March 2018,
Accepted 22nd June 2018

DOI: 10.1039/c8ee00936h

rsc.li/ees

We introduce five nickel phosphide compounds as electro-catalysts for the reduction of carbon dioxide in aqueous solution, that achieve unprecedented selectivity to C_3 and C_4 products (the first such report). Three products: formic acid (C_1), methylglyoxal (C_3), and 2,3-furandiol (C_4), are observed at potentials as low as +50 mV *vs.* RHE, and at the highest half-reaction energy efficiencies reported to date for any >C1 product (99%). The maximum selectivity for 2,3-furandiol is 71% (faradaic efficiency) at 0.00 V *vs.* RHE on Ni_2P, which is equivalent to an overpotential of 10 mV, with the balance forming methylglyoxal, the proposed reaction intermediate. P content in the series correlates closely with both the total C products and product selectivity, establishing definitive structure–function relationships. We propose a reaction mechanism for the formation of multi-carbon products, involving hydride transfer as the potential-determining step to oxygen-bound intermediates. This unlocks a new and more energy-efficient reduction route that has only been previously observed in nickel-based enzymes. This performance contrasts with simple metallic catalysts that have poor selectivity between multi-carbon products, and which require high overpotentials (>700 mV) to achieve comparable reaction rates.

Broader context

Electrochemical reduction of carbon dioxide (CO_2), powered by renewable electricity, is promising for producing clean fuels and chemical feedstocks in a sustainable cycle. Unfortunately, both sunlight and wind power are poorly correlated with consumer demand, hence requiring storage, *e.g.* as a fuel or chemical. CO_2 reduction using water as the hydrogen source may be carried out catalytically in electrolysers using power from either of these sources. However, low energy efficiencies and poor product selectivities reported so far prevent the commercial development of this technology. State-of-the-art copper catalysts produce hydrogen, plus a mixture of 16 carbon products at significant overpotentials. In this work we report for the first time the application of transition metal phosphides, specially a family of nickel phosphide catalysts, that surpass copper electro-catalysts and operate in ambient conditions in non-corrosive electrolytes. The best nickel phosphides operate at exceedingly low overpotential (~10 mV), yield no hydrogen by-product, and selectively form non-volatile C_3 and C_4 products. Both of the products, methylglyoxal and furandiol, can be used as precursors for polymers. Nickel phosphide catalysts are cheap, abundant, highly active, and could represent a breakthrough in the sequestration of CO_2 into fuels and chemical feedstocks for use in the polymer industry.

Introduction

The electrochemical reduction of carbon dioxide (CO_2 Reduction Reaction, CO_2RR) using water as hydrogen source has the potential to enable sustainable production of fuels, chemicals and polymers from renewable energy sources. While active and selective catalysts for CO_2 reduction to CO[1–7] and HCOOH[3,8–10] have been developed over the past few years, the generation of high-value multi-carbon products is not yet sufficiently efficient. Copper and alloys thereof are the only catalysts proven to generate C_2 and C_3 alkanes, alcohols, ketones and

[a] *Department of Chemistry and Chemical Biology, Rutgers, The State University of New Jersey, 610 Taylor Road, Piscataway, 08854 New Jersey, USA. E-mail: dismukes@rutgers.edu*
[b] *Waksman Institute of Microbiology, Rutgers, The State University of New Jersey, 190 Frelinghuysen Road, Piscataway, New Jersey, 08854, USA*

† Electronic supplementary information (ESI) available. See DOI: 10.1039/c8ee00936h

‡ These authors contributed equally.

aldehydes at significant rates.[11–24] However, copper-based catalysts are still limited by three problems: (1) poor selectivity of the reaction produces a wide range of carbon products, (2) high overpotentials waste energy to heat, and (3) significant H_2 co-production competes with the desired organic compounds.

Nørskov and co-workers have proposed a mechanism for the conversion of CO_2 to CH_4 on copper, based on density functional theory (DFT),[25] that involves initial reduction to adsorbed CO (*CO), which blocks surface H-adsorption sites and suppresses the significant competing hydrogen evolution reaction (HER). Their proposed potential-determining step (PDS) occurs when HCO* binds parallel to the Cu surface to create bonding interactions to both C and O atoms. The calculated PDS requires an applied potential of −0.74 V *vs.* RHE, which corresponds to the experimental onset of methane and ethylene production observed by Hori *et al.*[11] Since the PDS involves the binding of HCO*, the theoretical overpotential for methane formation should scale with the CO binding energy for different metal surfaces.[26] This descriptor is near the optimal value for copper, rationalizing its ranking as the best pure transition metal catalyst for reducing CO_2 beyond 2-electron reduction products.[14,26]

Binary materials that favor binding the HCO* intermediate through both the carbon and oxygen atoms should break the scaling relationships obeyed by simple metals and could potentially improve catalytic activity. Both nickel and phosphorous allow for increased stabilization of oxygen-bound intermediates, potentially decreasing the overpotential for reaction. Additionally, they form multiple binary compounds that can absorb hydrogen atoms which have different hydride bond strength (hydricity).[27–29] Moreover, the two principal enzymes that convert CO_2 to CO and subsequently couple C–C bonds, both utilize nickel in the active site. Both enzymes utilize sulfide + cyanide ligands to nickel, possibly to tune hydricity. Here, we approximate this ligand set using phosphorous which provides an iso-electronic replacement for the S + CN^- ligands. Nickel phosphides have been reported as highly active HER catalysts.[27–31] Using them for CO_2RR is contrary to the belief that effective catalysts should have poor HER activity, yet still efficiently transfer adsorbed hydrogen atoms to a *CO intermediate.[32] In contrast, other theoretical predictions by Rossmeisl *et al.*[33] claim that having hydrogen binding energy near thermo-neutral is critical for predicting the ability of pure metals to generate products beyond CO, and is equally as important as the *CO binding energy. This represents a shift in dogma for CO_2RR research and underscores the importance of reversible hydrogen binding for both HER and CO_2RR activities.

Based on these various insights, we synthesized a family of five nickel phosphide compounds: Ni_3P, Ni_2P, $Ni_{12}P_5$, Ni_5P_4, and NiP_2, and evaluated their performance as electrocatalysts for CO_2RR. Our results demonstrate that product selectivity greatly improves with increasing P content in this series. This is the first report of the formation of methylglyoxal (C3) and 2,3-furandiol (C4) products, with potential applications in the polymer industry. The best nickel phosphide catalyst achieves essentially complete discrimination over the HER, and an energy efficiency of 99% with the lowest overpotential reported thus far for any >C1 products.

Results and discussion

Catalyst crystallinity and purity

Compositional purity, crystal phase and crystal facet exposure are critical variables when comparing catalyst performance. Five different nickel phosphide compounds (Ni_3P, Ni_2P, $Ni_{12}P_5$, Ni_5P_4, and NiP_2) were synthesized by solid state reaction at 700 °C, in vacuum-sealed quartz tubes, using high purity elemental precursors. Comparison of the unique powder X-ray diffraction patterns to the nickel phosphide reference patterns (Fig. S1–S5, ESI†), verified that each was a single, pure phase, lacking contamination from secondary phases or amorphous material below the 2% detection limit. The nickel phosphides were intentionally synthesized at high temperature to achieve thermodynamic equilibrium among facets (*i.e.*, polycrystallinity). Polycrystallinity was confirmed by SEM analysis, showing particles with roughly spherical morphology, lacking distinct faceting, and with sizes ranging from 1–20 μm in diameter (Fig. S6, ESI†).

Electrolysis setup

The performance of polycrystalline electrocatalysts has, to date, been limited by the ability to consistently reproduce stable catalyst/electrode interfaces from powdered catalysts supported on conductors. Our group has developed a successful protocol for preparing electrodes from nickel phosphides by mixing them with a binder and pressing them into rigid pellets.[27,28] Due to the metallic nature of nickel phosphides,[27,28] no addition of conductive carbon was required. To obtain electrodes with a 2 cm diameter, the different polycrystalline powders were mixed with 1% (w/w) neutral Nafion™ (Sigma Aldrich 5 wt% solution in lower aliphatic alcohols and water, neutralized with 4 mg NaOH pellets per mL of solution). After grinding with a mortar and pestle until the solvent had evaporated, the mixture was transferred to an aluminum die containing an aluminum mesh for mechanical support (McMaster-Carr, 20 × 20 mesh size, 0.016″ wire diameter), then pressed at 7 ton per cm^2. The resulting pellets were porous and had a mean thickness of 575 μm (see ESI,† Fig. S7). The aluminum die was used directly as the working electrode support in a sandwich-type cell, depicted in Fig. 1. During the reaction, only the catalyst pellet was exposed to the electrolyte, and the back of the aluminum support was connected to the potentiostat. Aluminum was chosen for the support as it has been previously shown to have low activity for CO_2RR and HER.[34]

The use of relatively large and porous electrodes can lead to substantial iR-drop and significant errors in potential determination.[35] Resistive losses from the electrolyte were minimized by the use of a 0.5 M $KHCO_3$ buffer, resulting in a stable solution resistance of 6–8 ohms. Potentiostatic electrochemical impedance spectroscopy (PEIS) was performed before each experiment to measure the uncompensated resistance,

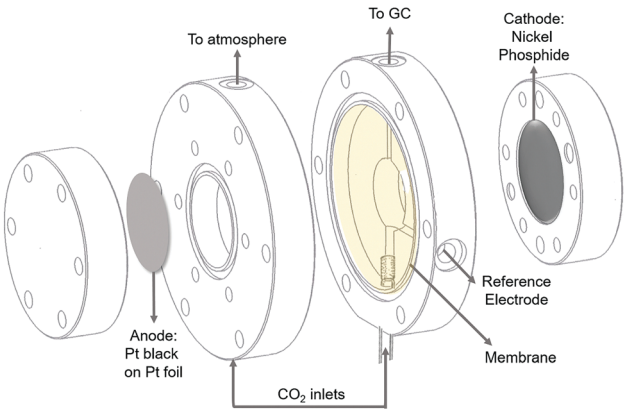

Fig. 1 Scheme of the sandwich-type electrochemical cell used. The cathode is nickel phosphide supported onto a die, separated from the anode by a Nafion membrane. The counter electrode is a Pt black@platinum foil. The electrolyte is purged from the bottom with CO_2 microbubbles and the headspace of the working electrode compartment is sampled by on-line gas chromatography.

which was used for positive feedback iR compensation (Fig. S7, ESI†). The solution resistance during the reactions consistently changed by less than 0.5 ohm (<2 mV). All potentials were measured against a commercial Hg/Hg_2SO_4 reference electrode, and converted to the thermodynamically relevant reversible hydrogen electrode (RHE) scale.

Avoiding gaseous CO_2 depletion is a concern for CO_2RR.[36,37] To minimize mass transport limitations, in addition to the carbonate buffer, CO_2 gas was fed through the bottom of the cell *via* a glass frit (4–8 μm pores), generating bubbles of 50 to 150 μm (measured by optical imaging). Such small bubble sizes are sufficient to ensure CO_2 saturation at operating currents lower than 10 mA cm^{-2}, as shown in a prior study by Lobaccaro *et al.*[37]

Gas-phase products were detected by an online gas chromatograph, using both thermal conductivity and flame ionization detectors, arranged in series. The working electrode had a large surface area (3.14 cm^2) to electrolyte volume (6 mL) ratio (S/V = 0.52 cm^{-1}) to maximize the concentration of liquid phase products in the electrolyte, in accordance with recent literature recommendations.[37,38] This allowed for direct product quantification by HPLC, that was further corroborated by NMR and LCMS analyses for unambiguous product assignments and yields (refer to ESI,† Fig. S12 and S13).

Table 1 Standard electrochemical potentials at pH 7.0

Product	Half-reaction	$E^{0'}$ (V *vs.* RHE)
Hydrogen	$2(e^- + H^+) \rightleftharpoons H_2$	0.00
Formic acid	$CO_2 + 2(e^- + H^+) \rightleftharpoons HCOOH$	−0.02
CO	$CO_2 + 2(e^- + H^+) \rightleftharpoons CO$	−0.10
Acetic acid	$CO_2 + 8(e^- + H^+) \rightleftharpoons H_3CCOOH$	+0.23
Methylglyoxal	$3CO_2 + 12(e^- + H^+) \rightleftharpoons C_3H_4O_2 + 4H_2O$	+0.02
2,3-Furandiol	$4CO_2 + 14(e^- + H^+) \rightleftharpoons C_4H_4O_3 + 5H_2O$	+0.01

CO_2 reduction products

Table 1 lists the reduction potentials ($E^{0'}$) and the number of electrons required to reduce CO_2 to various products, including the three products observed in this work (formate, methylglyoxal, and 2,3-furandiol). $E^{0'}$ at pH 7.0 *vs.* RHE was calculated from tabulated[39,40] thermodynamic data when available, and otherwise estimated by Mavrovouniotis' method of individual group contributions[41] (details in ESI,† Table S8). While formate is widely reported as a CO_2 reduction product,[3,8–10] this is the first report of the formation of methylglyoxal and 2,3-furandiol under electrochemical conditions. The $E^{0'}$ values reveal the latter products are thermodynamically easier to form than CO,

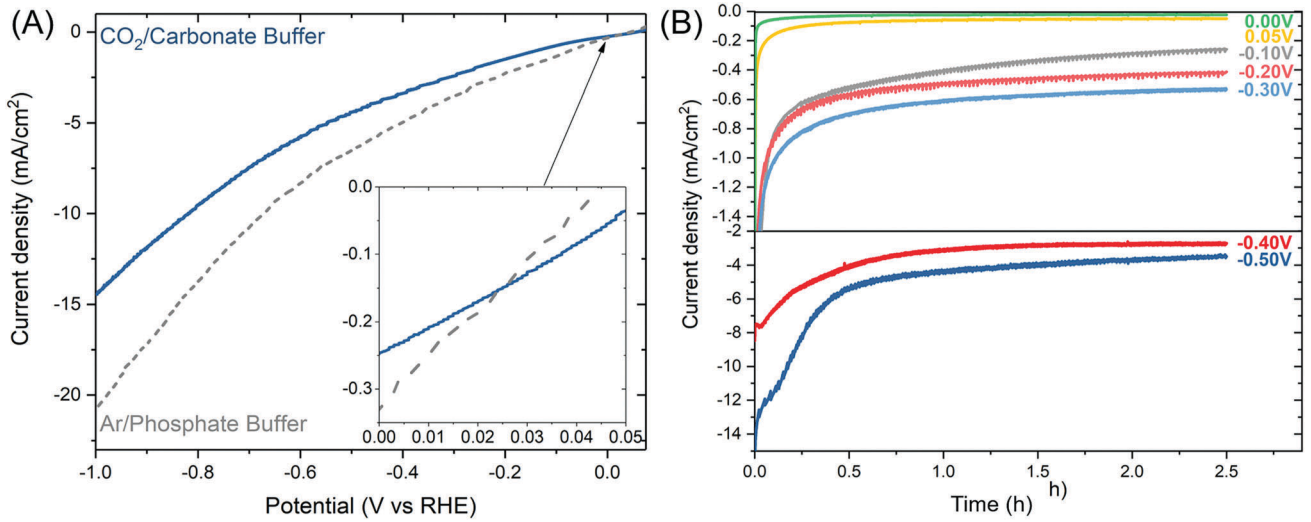

Fig. 2 (A) iR-corrected linear sweep voltammetry of Ni_2P at 0.5 mV s^{-1}. In grey, argon-purged 0.5 M phosphate buffer, pH 7.5. This current corresponds solely to the HER; in blue, CO_2-saturated 0.5 M $KHCO_3$, where the current is due to CO_2 reduction and HER. Binding of CO_2RR intermediates partially suppresses HER. Furthermore, the current for CO_2RR is seen to be larger than those attributed to HER in the phosphate buffer at low overpotentials (see inset). (B) Representative chronoamperometry measurements at different potentials for Ni_2P. Due to the high porosity of the catalyst, there is an initial charging period (as previously reported in acid and base[27]), after which the current stabilizes. Voltammetry and chronoamperometry for all stoichiometries can be found in the ESI,† Fig. S9.

formate, and H_2, suggesting a possible approach for selectivity. To test the origin of the carbon products, isotopic labeling with $^{13}CO_2$ as carbon source was conducted (refer to Fig. S14 in ESI†). This confirmed that dissolved CO_2 was indeed the sole source of carbon for C_1, C_3, and C_4 products. Control experiments using Ar-purged $KHCO_3$ electrolyte reduced the CO_2RR currents to 20% of their previous value, confirming that dissolved CO_2, rather than ionized forms of (bi)carbonate, is the main substrate for CO_2RR on nickel phosphides.

Current *vs.* potential

Fig. 2(A) presents voltammograms for Ni_2P, obtained using Ar saturated 0.5 M sodium phosphate buffer (grey), and CO_2 saturated 0.5 M $KHCO_3$ (blue), both at (pH 7.5). Under an argon atmosphere, the reductive current due to hydrogen evolution sharply increases with increasing overpotential.[27] In contrast, under CO_2 saturation, the current is suppressed at all negative potentials, indicating that CO_2RR intermediates bind to some or all of the same sites that would otherwise be active for HER. Most notably, at positive potentials, the observed current increases in the presence of CO_2, indicating that CO_2RR dominates. Four of the nickel phosphides express this behavior, with the exception of NiP_2, which reaches open circuit potential (OCP) below 0 *vs.* RHE (see ESI,† Fig. S9).

The stability of the catalyst current density was assessed by chronoamperometry, and is presented in Fig. 2(B) for Ni_2P (and for the remaining stoichiometries in the ESI,† Fig. S10).

The total current decreases in the first half hour of the experiment at all negative potentials (break-in period), due to the reduction of the surface phosphoxides, as well as the build-up of a pH gradient within the porous electrocatalyst, in agreement with our previous HER study using nickel phosphides.[30] After the initial break-in period, the current stabilizes, and no significant loss of CO_2 current activity is observed. The total charge passed in the break-in period amounts to less than 1% of the total charge that contributes to products. To measure corrosion resistance, dissolved nickel in the solution was quantified by ICP-OES. Less than 0.023% of the nickel in the catalyst was dissolved after 2.5 hours of electrolysis (see ESI,† Table S7), equivalent to trace amounts lost during reduction of the oxidized surface.

Selectivity *vs.* potential

Fig. 3 plots the faradaic efficiency of each product as a function of potential and catalyst composition. Reduction of CO_2 to 2,3-furandiol and methylglyoxal is predominant from 0.05 V to −0.10 V *vs.* RHE on the more phosphorus-rich nickel phosphides ($Ni_{12}P_5$, Ni_2P, Ni_5P_4, and NiP_2), with Ni_2P giving the highest faradaic yield at the lowest overpotential. In contrast, the low-phosphorous Ni_3P resulted in significantly less CO_2RR relative to HER and poorer selectivity, with more formic acid production than the other catalysts. The maximum selectivity of 84% for methylglyoxal was obtained on NiP_2 at −0.10 V. The reaction on NiP_2 was not performed at potentials more positive than −0.05 V *vs.* RHE because the catalyst reached OCP near 0 V, thus reducing the current and product formation below the

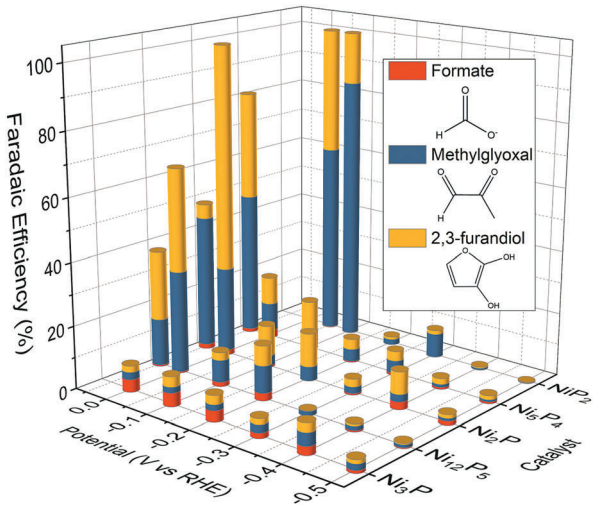

Fig. 3 Faradaic efficiency for CO_2RR as a function of potential and catalyst composition. The remaining faradaic efficiency is for H_2 (omitted for clarity). Electrolysis conducted in 0.5 M $KHCO_3$ (CO_2 saturated, pH 7.5). The three most phosphorus-rich stoichiometries, NiP_2, Ni_5P_4 and Ni_2P show selectivity for 2,3-furandiol and methylglyoxal at potentials between 0.05 V and −0.10 V.

detection limit. For 2,3-furandiol, the maximum faradaic efficiency of 71% was observed at 0 V *vs.* RHE on Ni_2P. Although formic acid is produced at all potentials, its faradaic efficiency never exceeds 5% for any of the catalysts. At more reductive potentials (< −0.2 V *vs.* RHE), the reaction selectivity shifts to HER. This behavior is in stark contrast with what is observed on copper catalysts,[38] where, at high overpotentials, hydrogen evolution is suppressed, and CO_2RR favored. This, along with the low overpotentials at which C–C coupling occurs, indicates that the mechanism of CO_2RR on nickel phosphides is radically different from those previously reported for simple metal catalysts.

Another important figure of merit is the CO_2RR current density that can be achieved, depicted in Fig. 4. In general,

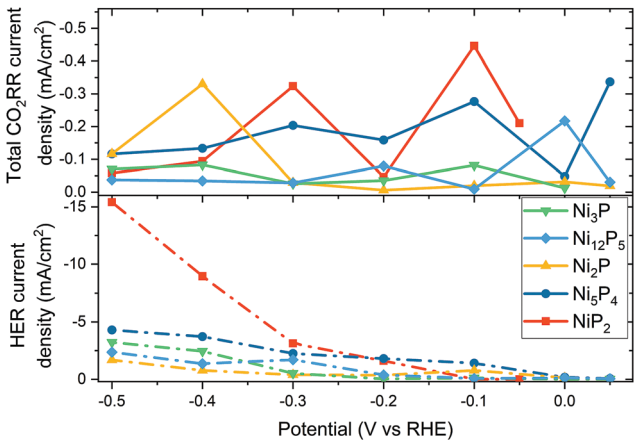

Fig. 4 Partial current densities obtained by the product of faradaic efficiency and current density at 3 hours of chronoamperometry. The total CO_2RR current is the sum of the partial current densities for 2,3-furandiol, methylglyoxal, and formic acid. Currents are normalized to the geometric surface area of the electrode. Lines are inserted only to guide the eye.

all catalysts except Ni_3P show distinct profiles with peaks indicative of discrete potentials that drive CO_2 reduction more efficiently, albeit at different peak potentials. The maximum CO_2RR specific current density from NiP_2 is -470 μA cm^{-2} at -0.05 V and a second substantial peak (-380 μA cm^{-2}) is evident at -0.3 V, suggestive of the population of two different electronic states. The former CO_2RR specific current density is twice that of polycrystalline copper for C_3 products at -1.1 V *vs.* RHE.[38] Only a single peak occurs on Ni_2P (-330 μA cm^{-2}) at -0.40 V *vs.* RHE, with currents that are ten fold lower at more positive potentials. For comparison, Ni_5P_4, which is notably the most active HER catalyst among the studied phases,[27,42] exhibits smaller CO_2RR currents across a broader range of potentials with peaks at -0.4 V (-200 μA cm^{-2}) and +0.05 V (-80 μA cm^{-2}). The latter peak is the highest CO_2RR activity among all the catalysts at this potential.

Table 2 Turnover frequency at the potential with maximum CO_2RR selectivity, based on electrochemical surface area

		Turnover frequency (10^{-6} mol of product/surface atom s)			
Catalyst	Potential (V *vs.* RHE)	$HCOO^-$	MG	FD	H_2
Ni_3P	-0.10	219	15.3	24.0	5119
$Ni_{12}P_5$	0.00	16.4	201	175	1281
Ni_2P	0.00	14.0	27.4	127	0
Ni_5P_4	+0.05	14.5	48.5	30.0	57.3
NiP_2	-0.10	2.16	204	68.5	0

Table 3 Energy efficiency of the CO_2RR at the potential with maximum selectivity, considering a perfect oxygen evolution anode

Catalyst	Potential (V *vs.* RHE)	CO_2RR energy efficiency (%)
Ni_3P	-0.10	8
$Ni_{12}P_5$	0.00	65
Ni_2P	0.00	99
Ni_5P_4	0.05	83
NiP_2	-0.10	92

Turnover frequencies (TOF) were determined by normalizing current density to electrochemical surface area and are listed in Table 2. TOF reveals the remarkable activity of NiP_2 and $Ni_{12}P_5$ for methylglyoxal (MG) production, while for Ni_2P and $Ni_{12}P_5$ the TOF for 2,3-furandiol (FD) production. The TOFs for MG and FD products on Ni_2P and NiP_2, respectively, are the most selective and, additionally, produce no H_2 at their peak potentials. By contrast, $Ni_{12}P_5$ has lower CO_2RR selectivity between these products and favors HER activity. Ni_3P produces mainly H_2 at all potentials and has low selectivity for CO_2RR, although its TOF for formate is the highest among the nickel phosphides. The TOFs for MG and FD on Ni_3P are of the same magnitude as the two main products, methane and ethylene, on polycrystalline copper, ($\sim 10^{-4}$ s^{-1} at -0.7 V *vs.* RHE) but at substantially larger overpotentials.[38]

Energy efficiency

Energy efficiency (ε_e) is a practical metric useful when comparing CO_2 reduction catalysts for energy storage applications, and is defined as the ratio of the thermoneutral potential (free energy) for each product to the applied electrical energy, eqn (1)[43]

$$\varepsilon_e = \sum(E^0 \times FE/E_{cell}) \quad (1)$$

Table 3 gives the energy efficiency for CO_2RR, assuming a perfect oxygen evolution catalyst at the anode. The values range

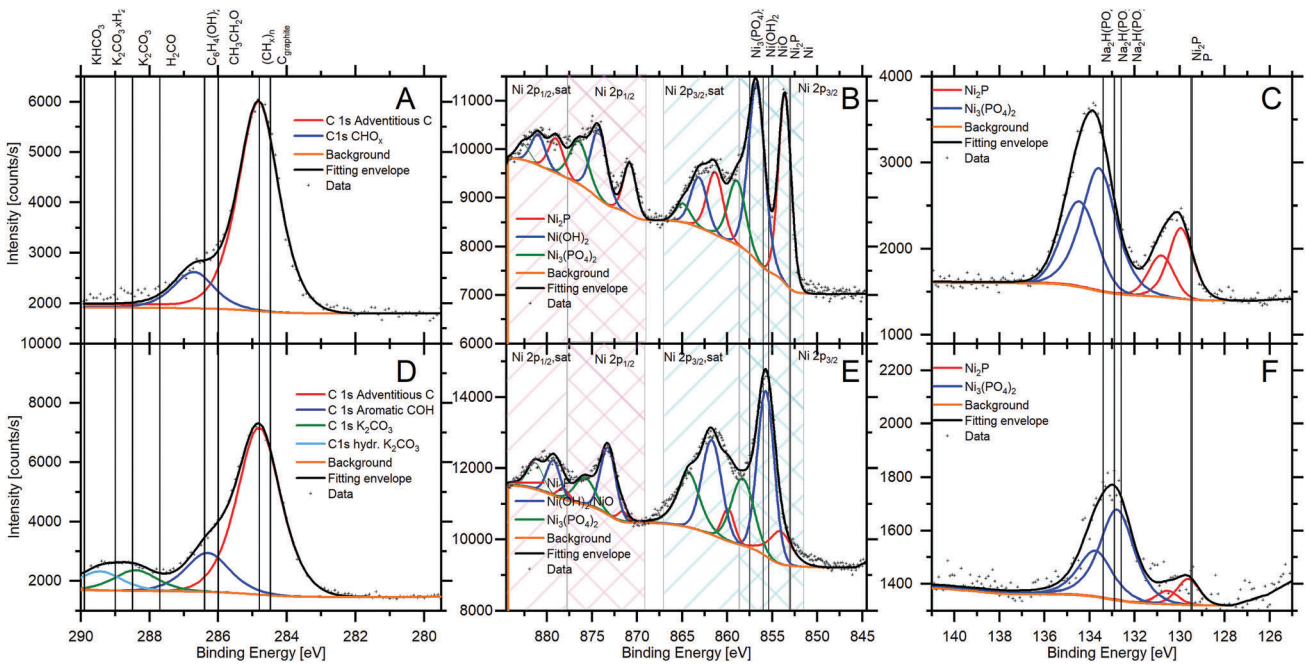

Fig. 5 XPS spectra of Ni_2P catalyst before and after CO_2RR (from left) C 1s, Ni 2p, and P 2p with fitted spectra. Top row is the analysis of the pristine catalyst; bottom row is the catalytically cycled material.

from 8% for Ni_3P to the maximum 99% for Ni_2P. For comparison, the energy efficiency is only 23% on polycrystalline copper.[38]

Surface changes following catalysis

The surface stability of all catalysts was further evaluated by X-ray photoelectron spectroscopy (XPS) before and after reaction. Fig. 5 presents the experimental and fitted XPS spectra for the Ni_2P catalyst (additional XPS results are shown in ESI,† Fig. S20–S24). XPS spectra are internally referenced to carbon (red peak) at a binding energy of 284.8 eV (see Fig. 5), and an additional peak (blue) from partially oxidized carbon (adventitious), which appears at the binding energy characteristic of aldehydes and terminal hydroxides.[44] Post-catalysis, the carbon peaks increase in intensity, along with the appearance of carbonate species (K 2p doublets from K_2CO_3 are also observed, see ESI†). Both carbonate and potassium binding energy shifts are also in agreement with the presence of hydrated and anhydrous K_2CO_3 (electrolyte) post-catalysis.[44,45] In the post-reaction of Ni_2P, the blue C 1s peak is shifted to a binding energy that could be attributed to aromatic carbons bound to hydroxide, such as those in 2,3-furandiol (reference for 1,2-dihydroxybenzene is shown).[44] This assignment is tentative as the peak could also be attributed to adventitious carbon that was not observed in the pristine catalyst.

The Ni 2p XPS spectra of Ni_2P (Fig. 5B and E) show the characteristic $2p_{3/2}$ and $2p_{1/2}$ doublets, each with corresponding satellite peaks. The Gaussian modelling shows that three distinct chemical species are present. The species are ascribed to $Ni^{\delta+}$ from Ni_2P and Ni^{2+} nickel hydroxide and/or oxide mixture ($Ni(OH)_2$/NiO), as well as Ni^{2+} from $Ni_3(PO_4)_2$.[44,46] This is in agreement with previous studies suggesting that nickel phosphides surface-oxidize to form a partially hydrated surface phosphate on top of the pristine nickel phosphide.[27,29] The surface phosphate layer thickness will be less than 1 nm, estimated by the probe depth of XPS in Ni(s). It should be noted that the relative content (estimated by peak height) of $Ni^{\delta+}$ relative to Ni^{2+} from the combined $Ni(OH)_2$/NiO and $Ni_3(PO_4)_2$ decreases upon catalytic turnover. When the catalyst is air-exposed post-catalysis, the surface re-oxidizes. The relative change indicates that the surface nickel oxide/phosphate thickness increases when oxidation occurs in the electrolyte, compared to oxidation in air post-synthesis. The latter conditions favor the formation of a hydroxylated surface phosphate.

The P 2p XPS spectrum of Ni_2P shows two sets of doublets in the $2p_{3/2}$ and $2p_{1/2}$ regions, which are ascribed to $P^{\delta-}$ and PO_4^{3-}. The ratio of $P^{\delta-}/PO_4^{3-}$ is seen to decrease after catalytic turnover, indicating that the surface phosphate has a higher degree of hydration post catalysis due to exposure to the electrolyte. The atomic ratio of $P^{\delta-}/Ni^{\delta+}$ is $\sim$1.9 both before and after catalytic turnover, respectively, and indicates that the catalyst composition does not change significantly in its reduced form (see ESI† for complete XPS analysis results).

After reaction, bulk changes were also evaluated by powder X-ray diffraction (ESI,† Fig. S1–S5). For Ni_3P, $Ni_{12}P_5$, Ni_2P, and Ni_5P_4, no detectable crystalline impurity was formed after catalysis ($<$2%). However, NiP_2, the most active catalyst, originally a pure monoclinic phase, partially converts (9%) to the cubic NiP_2 phase. Additionally, four minor peaks appear that could not be assigned based on XRD.

Reaction mechanism on nickel phosphides

Because all three reduction products are oxygenates, the C–C coupling step presumably occurs before the two carbon–oxygen bonds in CO_2 are broken. Additionally, the predominant formation of C–C coupling products implies that key reaction intermediates are bound to the catalyst by oxygen atom(s) rather than by the carbon atom, in contrast to the proposed mechanisms on catalysts that form formate as major product.[47]

Because the formation of all three products takes place at near-equilibrium potential, it is helpful to consider both thermodynamic and kinetic constraints on the possible reaction pathways to C–C coupling products. We consider the 2-electron reduction of CO_2 to formate first.

On formate-forming metals, where larger overpotentials are common, it is hypothesized that CO_2 binds through the oxygen atoms to the catalyst surface, upon the transfer of a single electron in a bent configuration followed by a proton-coupled electron transfer (PCET) to yield formate.[48] However, the equilibrium potential for the single electron transfer to form the radical anion is -1.45 V *vs.* RHE in aqueous media,[49] which is prohibitive for product formation in this study. More recently, it has been suggested that on metals such as tin, the first step of CO_2 reduction to formate is PCET,[50] as opposed to the single electron transfer suggested above. However, transition metals that are believed to operate through this mechanism still require strongly reducing potentials (-0.7 to -1.0 V *vs.* RHE).

Only a few catalysts are able to reduce CO_2 to $HCOO^-$ at near thermoneutral potential: the formate dehydrogenase enzyme,[51] thought to operate through hydride transfer ($CO_2 + H^- \rightarrow HCOO^-$)[52] and palladium-based materials,[8,10] which are also known to form active hydrides. DFT calculations of the hydrogen evolution reaction on Ni_2P, Ni_3P, and Ni_5P_4 indicate the presence of multiple types of hydride sites comprised of both Ni and P atoms at relevant potentials for HER and CO_2RR.[28,53–55] Notably, P sites are considered the most active for HER. These factors, together with the low potential at which the reaction operates, points to a hydride transfer mechanism for the initial step. This pathway is particularly favorable because the two-electron mechanism avoids the formation of high-energy radicals, both anionic CO_2^- and electro-neutral COOH. We next examine possible C–C coupling reactions that could generate methylglyoxal and 2,3-furandiol. Fig. 6 highlights the standard Gibbs free energy (ΔG^0) of a few possible reactions, calculated from tabulated values of ΔG^0 of formation[39–41] (see ESI,† Section S17). Standard free energy changes may guide the prediction of a suitable pathway even though the values may differ for non-standard conditions. The ΔG^0 for C–C coupling reactions becomes increasingly unfavorable in the sequence: reductive carboxylation of alcohols (-50 kJ mol^{-1} for methanol) $<$ self-condensation of aldehydes (-25 kJ mol^{-1} for formaldehyde) $<$ reductive CO coupling (+70 kJ mol^{-1}) $<$ the reduction of β-ketocarboxylic acids to ketoaldehyde (+100 kJ mol^{-1}) $<$ the

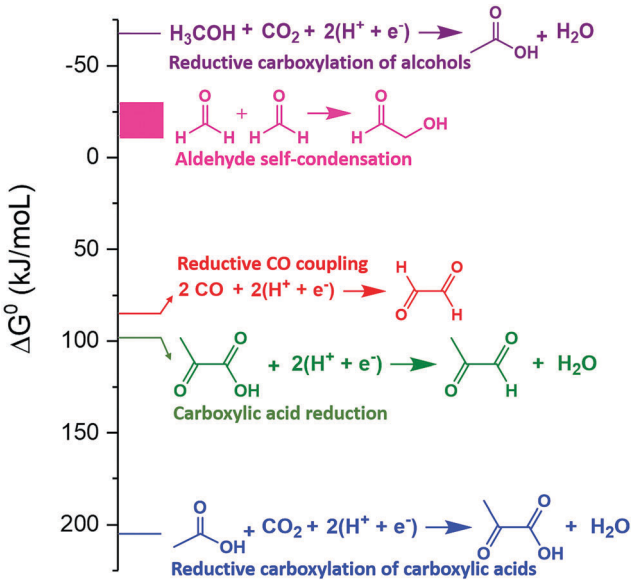

Fig. 6 Standard Gibbs free energy changes of possible carbon–carbon bond forming reactions at 298 K and pH 7.

carboxylation of carboxylic acids (+210 kJ mol^{-1} for acetic acid). Reductive coupling of CO units, while shown to be important for the formation of ethylene on copper at strongly reducing potentials,[48] is unlikely on nickel phosphides at low applied overpotentials, as the catalyst is highly oxophilic and selectively generates formate, not carbon monoxide. It should be noted that while the reductive carboxylation of methanol is highly exergonic, alcohols are kinetically very unreactive.[56] Therefore, the most energetically favored pathway for carbon–carbon coupling, under mild conditions in a bicarbonate buffer, is aldehyde self-condensation.

The literature on formaldehyde self-condensation to form trioses and tetroses suggests that the reaction is catalyzed by Lewis acids in the presence of water.[57] Binding of the carbonyl group of formaldehyde to a Lewis acid significantly lowers the barrier for proton abstraction from the C–H bond of formaldehyde, allowing C–C bond formation and producing glycolaldehyde. Nickel phosphides have Lewis acid character due to the partial positive charge on the nickel atoms, as shown in the XPS measurements (see Fig. 5B and E), and could catalyze this aldehyde condensation. CO_2 itself can also catalyze this condensation *via* carbonylation of nucleophilic oxides and phosphides.

One significant finding is that acetate is not formed, despite being thermodynamically favored (Table 1). This supports the aldehyde condensation pathway proposed, since forming C_3 products is both kinetically and thermodynamically favored.

Based on these steps, we propose that CO_2 reduction on nickel phosphides proceeds through the mechanism depicted in Fig. 7. In step 1, CO_2 inserts into a surface hydride bond to generate an adsorbed formate species, $*HCOO^-$. This is believed to be the potential-determining step (PDS) because the Tafel slopes for all three observed products are roughly the same (see ESI,† Fig. S19). We note that all three products are preceded by hydride exchange reactions with the surface, in steps 1, 2, and 10, and thus, the PDS for each product may be similar although chemically distinct steps. In step 2, formate is protonated and attacked by a second hydride, forming formaldehyde (H_2CO*) upon elimination of hydroxide. Although formaldehyde is not detected, it is highly reactive and presumably surface-bound to nucleophilic phosphide, whereupon two successive, energetically favored, aldehyde self-condensation reactions occur to generate glyceraldehyde. Step 6, the keto–enol tautomerization of an unactivated methyl group, is predicted to have the highest energy barrier, and thus accounts for the accumulation of the methylglyoxal precursor. This step is followed by another energetically favorable self-condensation of aldehyde with formaldehyde on the catalyst. The cyclization in step 8 forms a more stable five-membered ring by intramolecular condensation of an alcohol and an aldehyde. The hydride abstraction in step 10, the terminal product-forming reaction, is driven by the stability of the aromatic furan ring. There is precedent in literature for the hydride abstraction by nickel phosphides, as this is believed to be the mechanism for the thermally activated hydrodeoxygenation reaction that they are

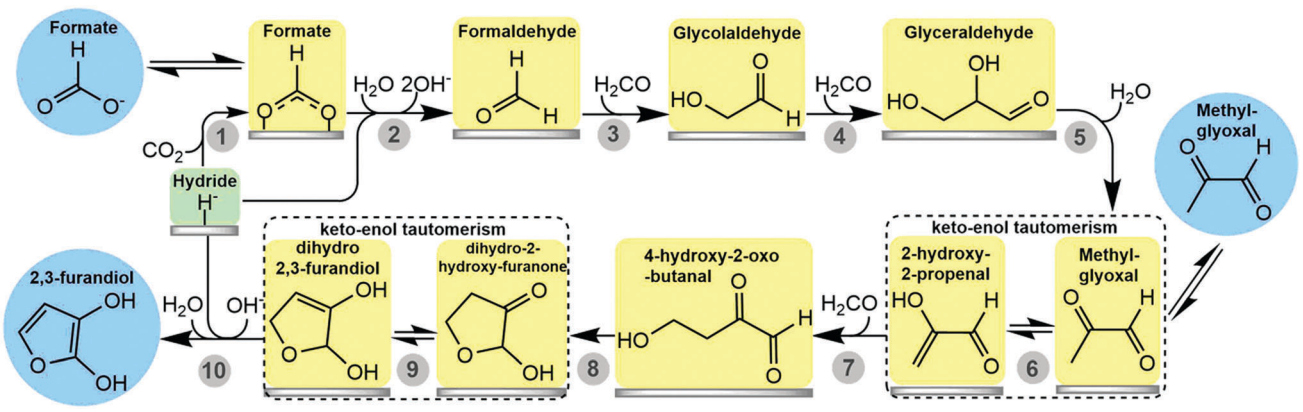

Fig. 7 The proposed reaction mechanism, that accounts for the three detected products highlighted in blue, for the electrocatalyzed reduction of CO_2 on nickel phosphides in concentrated dissolved bicarbonate electrolyte. The proposed surface-bound intermediates are highlighted in yellow. All intermediates are hypothesized to bind to the catalyst *via* oxygen atoms.

known to catalyze.[58] The proposed mechanism was validated by reduction of selected intermediates (formate, formaldehyde, methylglyoxal) as individual starting reagents in the absence of CO_2. In all cases, the resulting product distribution matched the expected end products in precisely the same stoichiometries observed when starting from CO_2 (refer to ESI,† Table S10).

The foregoing mechanism may account for the observed preference for P-rich nickel phosphides in forming C_3 and C_4 products, as these contain more of the nucleophilic P sites for binding both CO_2 and reactive hydride formation, the kind that exhibit nearly thermoneutral binding energy.[54,55] Such sites are favored to undergo CO_2 addition in the initial PDS, step 1. Surface reconstruction may contribute to the formation of additional P adatoms.[54,55] In particular, the theoretically predicted reconstruction of Ni_2P[001] produces a P-rich termination that is calculated to be highly nucleophilic.

Conclusions

This study demonstrates for the first time the use of transition metal phosphides for CO_2 reduction. Transition metal phosphides are the first class of materials, other than enzymes, that are able to convert CO_2 to C_3 and C_4 products in aqueous media at a near-thermoneutral potential with high selectivity, making them the best available electrocatalysts for forming $>C_2$ products. Copper is the only other non-biological catalyst that is able to produce multicarbon products with more than 1% faradaic efficiency. Five different nickel phosphide compounds examined here exceed this value, with NiP_2 the largest at 100%. When the kinetically facile HER reaction is discriminated against by using low overpotentials, the lowest energy C_n products appear. A strong structure-selectivity relationship favoring higher MW C_n products emerges among the five nickel phosphide catalysts as P content increases (NiP_2 most selective and Ni_3P least selective). Likewise, a strong structure–activity relationship between the integrated current producing C_n products and P content emerges. Each catalyst exhibits a different current–potential profile to form C_n products with distinct peaks. This is indicative of the population of discrete electronic states that form the key intermediates which produce these products. These relationships differ dramatically from pure metallic electrodes, notably copper. This study proposes a reaction pathway for the energy-efficient synthesis of multi-carbon chemicals from CO_2, *via* formate and formaldehyde intermediates, without the carbon monoxide intermediate formed when using pure metallic electrodes. Future work will focus on expansion of the mechanistic understanding of this reaction, as well as electrode engineering and catalyst development to improve current densities to industrially relevant values.

Experimental

Catalyst synthesis

Nickel metal powder (Sigma Aldrich, 99.99%, <150 μm) was mixed with stoichiometric amounts, plus 1.5% molar excess, of red phosphorus (Alfa Aesar, 98.9%, 100 mesh). The powders were ground with an agate mortar and pestle for 10 min, transferred to a quartz tube, then flushed with argon and evacuated to less than 100 mTorr three times. The evacuated quartz tubes contained batches of $\sim$5 grams of sample, which were sealed and heated at a rate of 0.5 °C min^{-1} stepwise (350 °C, 450 °C, and 550 °C) to 700 °C. The temperature was maintained for 6 hours at each intermediate step, and 24 h at the final temperature (to avoid hotspot formation due to the exothermic reaction). The powders were then analyzed by PXRD and, if not phase-pure, excess phosphorus or nickel was added and the procedure repeated as many times as necessary. The synthesized Ni_3P contained excess metallic nickel, which was removed by stirring with 10% HCl under nitrogen for 12 hours, and by washing with copious amounts of water. The acid wash was repeated as many times as necessary for complete removal of Ni, verified by PXRD.

Powder X-ray diffraction

Powder X-ray diffraction was conducted at room temperature on a Philips Xpert system, spinning at 100 rpm, in a Bragg–Brentano geometry, Cu K-alpha 0.15418 nm, calibrated daily with a Si standard. The step size used for the diffraction patterns was 0.02°, and the scan speed was 0.013° s^{-1}. The sample holder was 3 mm deep and $\frac{1}{2}''$ in diameter.

Electrochemistry

Each CO_2RR faradaic efficiency value reflects the average of at least 3 replicates. The standard deviation between HPLC measurements was smaller than 2%. The cell used was a custom-made glass-reinforced nylon-6,6 electrochemical cell, with silicon O-rings and PEEK fittings (IDEX HS). The working electrode was separated from the counter electrode by a Nafion 115 membrane (Fuel Cell Store). Platinum black deposited on Pt foil (Alfa Aesar, 99.9%) was utilized as the counter electrode. The Hach Hg/Hg_2SO_4 reference electrode was calibrated daily against a pristine Accumet SCE electrode. This SCE was periodically calibrated against a freshly flame-annealed Pt electrode in 0.5 M H_2SO_4 under 1 atm H_2 to calibrate to the RHE scale. The working electrode was prepared by mixing 1.400 g of the catalyst with 1% (w/w) neutralized Nafion suspension and was then pressed at 22 ton onto an aluminum die. The die, containing the pressed catalyst pellet was employed directly as the working electrode and current collector, with only the nickel phosphide exposed to the electrolyte. Aluminum was selected as a support because it is inert for CO_2RR.[34] CO_2 (Air Gas, instrument grade, with a Supelco hydrocarbon trap) was supplied through the bottom of the cell to both the working and counter electrodes at a flow rate of 5 sccm (certified MKS P4B mass flow controllers). The headspace of the working electrode compartment was sampled every 30 minutes for gas chromatography.

Electrochemical measurements were performed with a Gamry 5000E potentiostat. Before each electrolysis, the electrolyte (0.5 M $KHCO_3$, Chelex treated) was pre-saturated with CO_2 for at least an hour. Then, a chromatograph was taken to ensure that no air was present in the headspace. An electrochemical

impedance spectrum at the open circuit from 1 Hz to 1 MHz was taken to find out the uncompensated resistance (typically between 6 and 11 ohm). Chronoamperometry was then performed for 3 hours with positive feedback IR compensation. Between experiments, the electrochemical cell was rinsed with Millipore water and the working electrode catalyst pellet was lightly polished with a fine-grit silicon carbide polishing pad (BASi) before being re-used for multiple experiments at all potentials. In doing this, the longevity of the electrodes was confirmed, with no significant difference in product distribution observed as the electrodes were re-used. Additional replicas were made using fresh electrodes at all potentials to ensure that the product distribution was not affected across the investigated potential region.

Gas chromatography

Detection and quantification of possible headspace products (hydrogen, carbon monoxide, carbon dioxide, methane, ethane, and ethylene) was performed by an auto-sampling online HP 5890 Series II GC, with a 500 μL sample loop. The GC was fitted with a 6′ packed HayeSep D, and a 6′ packed MoleSieve 13× column, with thermal conductivity and flame ionization detectors connected in series. Samples were taken before reaction to check for air presence, and then every 30 minutes thereafter. Calibration curves were constructed from certified gas standards (Gasco) by CO_2 dilution using mass flow controllers (MFCs). The hydrogen calibration was done with *in situ* generated gas through electrolysis of water on platinum, under argon (supplied by an MFC), and diluted post-reaction with CO_2.

High-performance liquid chromatography (UV/RID)

Liquid products were identified and quantified on a Perkin-Elmer Flexar HPLC equipped with an auto-sampler, refractive index (RID) and UV-vis detector. An HPX 87H Aminex column (BioRad) was used, with injection volumes of 20 μL. The runtime was 60 minutes at a flow rate of 0.3 mL min^{-1} and 35 °C. Calibration ($R^2 > 0.999$) was conducted with standards of concentrations between 0.1–50 mM. The standards were: formaldehyde, glycerol, ethylene glycol, methanol, and ethanol, in 0.5 M $KHCO_3$, detected using the RID. Acetic acid, formic acid, citric acid, oxalate, malic acid, and succinic acid standards were prepared at concentrations of 0.01–5 mM and detected by UV at 210 nm. Product assignment was confirmed by ^1H NMR and LC-MS, as described in detail in the ESI.†

Conflicts of interest

There are no conflicts to declare.

Acknowledgements

This work was supported by Rutgers TechAdvance through grant 205718. K. U. D. C. thanks the BASF Catalysis Division for a generous fellowship. A. B. L. gratefully acknowledges funding from Rutgers, NSF-CBET/EERE grant #CBET-1433492 and DOE-EERE-FCTO grant #EE0008083. K. M. K. Y., T. A. G. and A. L. acknowledge support from the Aresty Undergraduate Research Institute. T. A. G. thanks the Rutgers Energy Institute for Summer support. G. C. D. thanks support received from the Pray Family Fund.

References

1 B. Kumar, M. Asadi, D. Pisasale, S. Sinha-Ray, B. A. Rosen, R. Haasch, J. Abiade, A. L. Yarin and A. Salehi-Khojin, *Nat. Commun.*, 2013, **4**, 2819.
2 B. A. Rosen, a. Salehi-Khojin, M. R. Thorson, W. Zhu, D. T. Whipple, P. J. A. Kenis and R. I. Masel, *Science*, 2011, **334**, 643–644.
3 J. Medina-Ramos, R. C. Pupillo, T. P. Keane, J. L. DiMeglio and J. Rosenthal, *J. Am. Chem. Soc.*, 2015, **137**, 5021–5027.
4 Y. Chen, C. W. Li and M. W. Kanan, *J. Am. Chem. Soc.*, 2012, **134**, 19969–19972.
5 W. Zhu, Y.-J. Zhang, H. Zhang, H. Lv, Q. Li, R. Michalsky, A. A. Peterson and S. Sun, *J. Am. Chem. Soc.*, 2014, **136**, 16132–16135.
6 M. Liu, Y. Pang, B. Zhang, P. De Luna, O. Voznyy, J. Xu, X. Zheng, C. T. Dinh, F. Fan, C. Cao, F. P. G. de Arquer, T. S. Safaei, A. Mepham, A. Klinkova, E. Kumacheva, T. Filleter, D. Sinton, S. O. Kelley and E. H. Sargent, *Nature*, 2016, **537**, 382–386.
7 J. Wu, R. M. Yadav, M. Liu, P. P. Sharma, C. S. Tiwary, L. Ma, X. Zou, X.-D. Zhou, B. I. Yakobson, J. Lou and P. M. Ajayan, *ACS Nano*, 2015, **9**, 5364–5371.
8 A. Klinkova, P. De Luna, C. T. Dinh, O. Voznyy, E. M. Larin, E. Kumacheva and E. H. Sargent, *ACS Catal.*, 2016, **6**, 8115–8120.
9 S. Gao, Y. Lin, X. Jiao, Y. Sun, Q. Luo, W. Zhang, D. Li, J. Yang and Y. Xie, *Nature*, 2016, **529**, 68–71.
10 R. Kortlever, I. Peters, S. Koper and M. T. M. Koper, *ACS Catal.*, 2015, **5**, 3916–3923.
11 Y. Hori, K. Kikuchi, A. Murata and S. Suzuki, *Chem. Lett.*, 1986, 897–898.
12 D. Ren, N. T. Wong, A. D. Handoko, Y. Huang and B. S. Yeo, *J. Phys. Chem. Lett.*, 2016, **7**, 20–24.
13 D. Ren, Y. Deng, A. D. Handoko, C. S. Chen, S. Malkhandi and B. S. Yeo, *ACS Catal.*, 2015, **5**, 2814–2821.
14 Y. Hori, H. Wakebe, T. Tsukamoto and O. Koga, *Electrochim. Acta*, 1994, **39**, 1833–1839.
15 C. S. Chen, A. D. Handoko, J. H. Wan, L. Ma, D. Ren and B. S. Yeo, *Catal. Sci. Technol.*, 2015, **5**, 161–168.
16 Y. Li, F. Cui, M. B. Ross, D. Kim, Y. Sun and P. Yang, *Nano Lett.*, 2017, **17**, 1312–1317.
17 H. S. Jeon, S. Kunze, F. Scholten and B. Roldan Cuenya, *ACS Catal.*, 2017, 531–535.
18 Y. Hori, A. Murata and R. Takahashi, *J. Chem. Soc., Faraday Trans. 1*, 1989, **85**, 2309.
19 R. Kas, R. Kortlever, H. Yılmaz, M. T. M. Koper and G. Mul, *ChemElectroChem*, 2015, **2**, 354–358.
20 Y. Song, R. Peng, D. K. Hensley, P. V. Bonnesen, L. Liang, Z. Wu, H. M. Meyer, M. Chi, C. Ma, B. G. Sumpter and A. J. Rondinone, *ChemistrySelect*, 2016, **1**, 6055–6061.

21 Y. Kwon, Y. Lum, E. L. Clark, J. W. Ager and A. T. Bell, *ChemElectroChem*, 2016, **3**, 1012–1019.
22 K. Zhao, Y. Liu, X. Quan, S. Chen and H. Yu, *ACS Appl. Mater. Interfaces*, 2017, **9**, 5302–5311.
23 A. Dutta, M. Rahaman, N. C. Luedi, M. Mohos and P. Broekmann, *ACS Catal.*, 2016, **6**, 3804–3814.
24 C. S. Chen, J. H. Wan and B. S. Yeo, *J. Phys. Chem. C*, 2015, **119**, 26875–26882.
25 A. A. Peterson, F. Abild-Pedersen, F. Studt, J. Rossmeisl and J. K. Nørskov, *Energy Environ. Sci.*, 2010, **3**, 1311.
26 A. A. Peterson and J. K. Nørskov, *J. Phys. Chem. Lett.*, 2012, **3**, 251–258.
27 A. B. Laursen, K. R. Patraju, M. J. Whitaker, M. Retuerto, T. Sarkar, N. Yao, K. V. Ramanujachary, M. Greenblatt and G. C. Dismukes, *Energy Environ. Sci.*, 2015, **8**, 1027–1034.
28 A. B. Laursen, R. B. Wexler, M. J. Whitaker, E. J. Izett, K. U. D. Calvinho, S. Hwang, R. Rucker, H. Wang, J. Li, E. Garfunkel, M. Greenblatt, A. M. Rappe and G. C. Dismukes, *ACS Catal.*, 2018, **8**, 4408–4419.
29 E. J. Popczun, J. R. McKone, C. G. Read, A. J. Biacchi, A. M. Wiltrout, N. S. Lewis and R. E. Schaak, *J. Am. Chem. Soc.*, 2013, **135**, 9267–9270.
30 Z. Huang, Z. Chen, Z. Chen, C. Lv, H. Meng and C. Zhang, *ACS Nano*, 2014, **8**, 8121–8129.
31 P. Jiang, Q. Liu and X. Sun, *Nanoscale*, 2014, **6**, 13440–13445.
32 A. A. Peterson and J. K. Nørskov, *J. Phys. Chem. Lett.*, 2012, **3**, 251–258.
33 A. Bagger, W. Ju, A. S. Varela, P. Strasser and J. Rossmeisl, *ChemPhysChem*, 2017, **18**, 3266–3273.
34 K. P. Kuhl, PhD thesis, Stanford University, 2013.
35 D. van der Vliet, D. S. Strmcnik, C. Wang, V. R. Stamenkovic, N. M. Markovic and M. T. M. Koper, *J. Electroanal. Chem.*, 2010, **647**, 29–34.
36 J. T. Billy and A. C. Co, *ACS Catal.*, 2017, **7**, 8467–8479.
37 P. Lobaccaro, M. R. Singh, E. L. Clark, Y. Kwon, A. T. Bell and J. W. Ager, *Phys. Chem. Chem. Phys.*, 2016, **18**, 26777–26785.
38 K. P. Kuhl, E. R. Cave, D. N. Abram and T. F. Jaramillo, *Energy Environ. Sci.*, 2012, **5**, 7050.
39 D. R. Lide, *CRC Handbook of Chemistry and Physics*, CRC Press, 84th edn, 2004.
40 A. J. Bard, R. Parsons and J. Jordan, *Standard Potentials in Aqueous Solutions*, International Union of Pure and Applied Chemistry, New York, NY, 1985.
41 M. L. Mavrovouniotis, *J. Biol. Chem.*, 1991, **266**, 14440–14445.
42 Y. Pan, Y. Liu, J. Zhao, K. Yang, J. Liang, D. Liu, W. Hu, D. Liu, Y. Liu and C. Liu, *J. Mater. Chem. A*, 2015, **3**, 1656–1665.
43 G. O. Larrazábal, A. J. Martín and J. Pérez-Ramírez, *J. Phys. Chem. Lett.*, 2017, 3933–3944.
44 A. V. Naumkin, A. Kraut-Vass, S. W. Gaarenstroom and C. J. Powell, NIST X-Ray Photoelectron Spectroscopy Database, https://srdata.nist.gov/xps/Default.aspx, accessed 1 January 2017.
45 A. Shchukarev and D. Korolkov, *Open Chem.*, 2004, **2**, 347–362.
46 K. Rokosz, T. Hryniewicz and S. Raaen, *Teh. Vjesn. – Tech. Gaz.*, 2017, **24**, 193–198.
47 C. W. Machan, S. A. Chabolla, J. Yin, M. K. Gilson, F. A. Tezcan and C. P. Kubiak, *J. Am. Chem. Soc.*, 2014, **136**, 14598–14607.
48 R. Kortlever, J. Shen, K. J. P. Schouten, F. Calle-Vallejo and M. T. M. Koper, *J. Phys. Chem. Lett.*, 2015, **6**, 4073–4082.
49 P. S. Surdhar, S. P. Mezyk and D. A. Armstrong, *J. Phys. Chem.*, 1989, **93**, 3360–3363.
50 J. T. Feaster, C. Shi, E. R. Cave, T. Hatsukade, D. N. Abram, K. P. Kuhl, C. Hahn, J. K. Nørskov and T. F. Jaramillo, *ACS Catal.*, 2017, 4822–4827.
51 T. Reda, C. M. Plugge, N. J. Abram and J. Hirst, *Proc. Natl. Acad. Sci. U. S. A.*, 2008, **105**, 10654–10658.
52 R. A. Torres, B. Schiøtt and T. C. Bruice, *J. Am. Chem. Soc.*, 1999, **121**, 8164–8173.
53 P. Liu and J. A. Rodriguez, *J. Am. Chem. Soc.*, 2005, **127**, 14871–14878.
54 R. B. Wexler, J. M. P. Martirez and A. M. Rappe, *ACS Catal.*, 2017, **7**, 7718–7725.
55 R. B. Wexler, J. M. P. Martirez and A. M. Rappe, *Chem. Mater.*, 2016, **28**, 5365–5372.
56 S. Ramayya, A. Brittain, C. DeAlmeida, W. Mok and M. J. Antal, *Fuel*, 1987, **66**, 1364–1371.
57 S. Thripati and R. O. Ramabhadran, *J. Phys. Chem. A*, 2017, **121**, 8659–8674.
58 P. Bui, J. A. Cecilia, S. T. Oyama, A. Takagaki, A. Infantes-Molina, H. Zhao, D. Li, E. Rodríguez-Castellón and A. Jiménez López, *J. Catal.*, 2012, **294**, 184–198.